Optics Letters

Widely tunable 2 μm hybrid laser using GaSb semiconductor optical amplifiers and a Si_3N_4 photonics integrated reflector

Nouman Zia,* Samu-Pekka Ojanen, Jukka Viheriala, Eero Koivusalo, Joonas Hilska, Heidi Tuorila, and Mircea Guina

Optoelectronics Research Centre, Physics Unit, Tampere University, Korkeakoulunkatu 3, 33720, Finland
**Corresponding author: nouman.zia@tuni.fi*

Received 21 November 2022; revised 12 January 2023; accepted 31 January 2023; posted 1 February 2023; published 1 March 2023

Tunable lasers emitting in the 2–3 μm wavelength range that are compatible with photonic integration platforms are of great interest for sensing applications. To this end, combining GaSb-based semiconductor gain chips with Si_3N_4 photonic integrated circuits offers an attractive platform. Herein, we utilize the low-loss features of Si_3N_4 waveguides and demonstrate a hybrid laser comprising a GaSb gain chip with an integrated tunable Si_3N_4 Vernier mirror. At room temperature, the laser exhibited a maximum output power of 15 mW and a tuning range of ~90 nm (1937–2026 nm). The low-loss performance of several fundamental Si_3N_4 building blocks for photonic integrated circuits is also validated. More specifically, the single-mode waveguide exhibits a transmission loss as low as 0.15 dB/cm, the 90° bend has 0.008 dB loss, and the 50/50 Y-branch has an insertion loss of 0.075 dB.

https://doi.org/10.1364/OL.480867

Photonics integration has been widely recognized as a major driving force fostering the development of new photonics applications, including data center transceivers, wearable sensors for health monitoring, and solid-state light detection and ranging (lidar) solutions. In fact, tailored multi-functional photonic integrated circuits (PICs) are the key building blocks enabling many new applications. PICs bring important benefits for volume scaling at affordable costs, miniaturization, and improved reliability. These benefits have been widely exploited by combining silicon photonics with InP-based gain chips for complex high-bandwidth optical transceivers [1,2] operating at telecom wavelengths. While the established PIC platform finds use in other applications, it provides marginal coverage for the 2–3 μm wavelength window required for sensing applications, such as the sensing of atmospheric pollutants [3,4] or the real-time monitoring of glucose levels [5], to name a few. These types of applications require a tunable narrow-bandwidth light source to be able to investigate multiple complex spectral fingerprints spanning a broad spectral band [6].

To date, PIC-based tunable hybrid external-cavity lasers near the 2 μm range have been largely based on the submicron silicon-on-insulator (SOI) platform [7–9]. This limits the extension of the technology toward 3 μm due to high mode leakage into lossy SiO_2 bottom and top claddings [10]. The silicon platform is also not ideal for high-power applications due to the two-photon absorption in the wavelength range between 1.55 and 2 μm. Moreover, the limited performance of the InP material system in this wavelength range has restricted the development of InP/SOI PICs up to 2.35 μm [9]. Alternatively, silicon nitride (Si_3N_4) has been hailed as a promising integrated photonics platform [11–13] offering ultralow propagation losses, negligible nonlinear absorption, and a wide transparency window extending from the visible to the mid-IR. This platform offers a low index contrast between the Si_3N_4 waveguide and the SiO_2 cladding, which is a benefit as it allows higher fabrication tolerances for waveguide circuitry. Furthermore, on-chip sensors relying on an evanescent coupling scheme become more sensitive when low contrast between the waveguide and air enables greater interaction between the propagating light and the environment or functionalized surfaces. In terms of III-V gain materials matching the spectral needs, GaInAlAsSb/GaSb-based type-I laser diodes have excelled in the 2–3 μm wavelength range [14–16], as they ensure high gain at relatively low thresholds and a low operation voltage, in particular around 2 μm.

In this Letter, we report, for the first time to the best of our knowledge, the use of a Si_3N_4-PIC Vernier reflector for locking and tuning the wavelength of a 2 μm hybrid laser incorporating a GaSb type-I quantum well heterostructure. We deployed a relatively thick (800 nm) Si_3N_4 platform to prevent mode overlap with the cladding. The demonstrated hybrid laser shows the potential of this platform for chip-scale tunable lasers at 2 μm wavelength and beyond. In particular, a record wide tuning range of ~90 nm (1937–2026 nm) and a relatively high output power of 15 mW are demonstrated for room-temperature operation. We further discuss the design of the Si_3N_4 Vernier PIC and explore in detail the loss performance enabling further wavelength scaling.

Figure 1(a) shows a detailed schematic diagram of the integrated hybrid laser, which consists of a 2-mm-long ridge

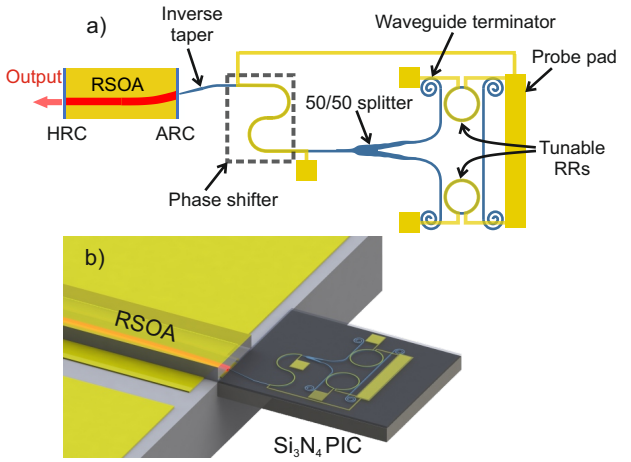

Fig. 1. (a) Detailed schematic of the widely tunable laser design, showing the RSOA gain chip and Si_3N_4 Vernier mirror together with important PIC building blocks and (b) 3D illustration of the hybrid laser.

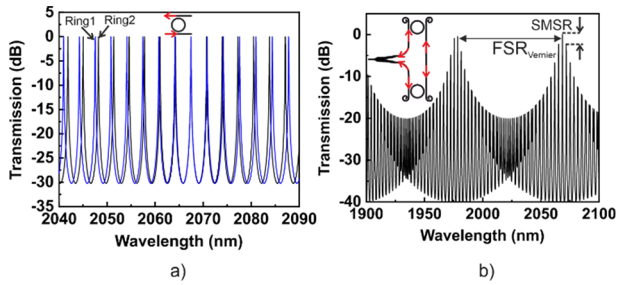

Fig. 2. Theoretical transmission spectra of (a) two RRs with slightly different FSRs and (b) the Vernier filter.

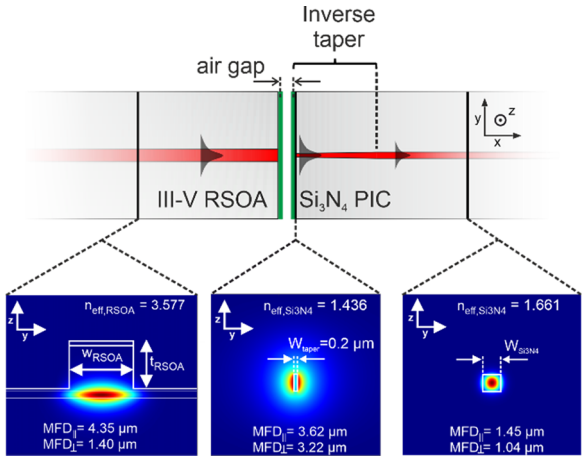

Fig. 3. Schematic of the edge-coupling interface between the RSOA gain chip and the Si_3N_4 PIC, together with simulated 2D fundamental TE mode profiles of the RSOA waveguide ($W_{RSOA} = 5$ μm, $t_{RSOA} = 2076$ nm), the Si_3N_4 waveguide at the taper input ($W_{taper} = 0.2$ μm), and the Si_3N_4 waveguide at the output ($W_{Si3N4} = 1$ μm). $MFD_{\perp}$ = mode field diameter vertical, $MFD_{\parallel}$ = mode field diameter horizontal.

waveguide (RWG) reflective semiconductor optical amplifier (RSOA) end-fire coupled with a Si_3N_4 Vernier PIC. The RSOA heterostructure was grown via molecular beam epitaxy (MBE) on a (100) n-GaSb substrate. The active region consists of 10-nm-thick In(0.25)GaSb type-I double quantum wells embedded in lattice-matched 260 nm Al(0.25)GaAsSb waveguide and 10 nm barrier layers. The waveguide is sandwiched between 2000-nm-thick p- and 2700-nm-thick n-Al(0.50)GaAsSb claddings. The heterostructure was processed into a 5-μm-wide (W_{RSOA}) and 2076-nm-deep (t_{RSOA}) RWG geometry targeted for single-transverse-mode operation. The coupling facet of the RSOA RWG was tilted 7° and anti-reflection coated (ARC) to suppress lasing in the RSOA and to obtain a broad spectrum. The rear (output) facet of the RSOA was high-reflection coated (HRC). Figure 1(b) is a 3D illustration of a hybrid coupling scheme between RSOA and Si_3N_4 PIC.

The Vernier PIC was realized on a LIGENTEC 800-nm-thick Si_3N_4 platform through open-access foundry services [17], and each component was optimized using the Ansys Lumerical software suite [18] for low-loss broadband operation around 2 μm. The 1-μm-wide strip waveguides were designed for low-loss (0.05 dB/cm) single-transverse-mode operation. The PIC coupling interface consists of an ARC waveguide with an inverse taper edge coupler to maximize the coupling efficiency. The inverse taper is tilted at 17° to match the output angle of the RSOA. An ultralow-loss (~0.05 dB), broadband (>200 nm), and small-footprint (34 μm × 7 μm) 50/50 Y-branch splitter was designed through the Ansys Lumerical Photonic Inverse Design (PID) package to split the light into two arms. Each arm includes a ring resonator (RR), forming a single-pass loop mirror. The light travels through the two RRs, which have slightly different radii, leading to the Vernier effect [19]. In this design, the RR radii were chosen to be 100 μm and 96.7 μm, which corresponds to free spectral ranges (FSRs) of 3.03 nm and 3.13 nm [20] for a group index of 2.09. Figure 2(a) shows the simulated transmission response for the two lossless RRs with a coupling coefficient of 0.04 between the ring and the bus waveguide. The simulated Vernier transmission [Fig. 2(b)], which is the overlap between the spectral responses of both RRs, gives rise to an FSR of 90 nm for our design. Metal heaters were added onto the ring waveguides to tune the Vernier transmission covering the full FSR. A thermal phase shifter (PS) was also added in the PIC to align the cavity resonance with the Vernier resonance, i.e., the Si_3N_4 PIC and RSOA are perfectly phase matched. Spiral waveguides were placed at the through ports of each RR to suppress back reflections. The PIC waveguide bends, with a radius of 100 μm, were designed for a negligible loss of 0.003 dB/90°.

The RSOA–PIC coupling interface consists of an inverse taper edge coupler to maximize the coupling efficiency. A schematic of the coupling interface between the RSOA and the Si_3N_4 PIC with an inverse taper is shown in Fig. 3. The cross-sectional optical field simulations performed with Ansys Lumerical Finite-Difference Eigenmode (FDE) are also shown in Fig. 3. The simulation represents the fundamental transverse electric (TE) modes of the RSOA waveguide, the Si_3N_4 waveguide at the taper input, and the Si_3N_4 waveguide at the taper output, along with their mode field diameters (MFDs) and the effective index (n_{eff}).

Figure 4(a) shows the simulated mode mismatch loss between the fundamental TE modes of the RSOA and the Si_3N_4 taper input for a fixed RSOA geometry and varying Si_3N_4 taper input widths. The simulations were performed with the Ansys Lumerical FDE solver. The results reveal that a minimum mode

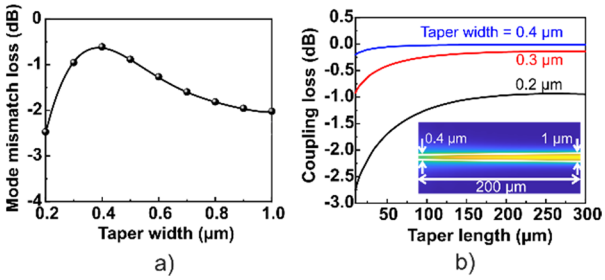

Fig. 4. (a) Simulated mode mismatch loss between the RSOA and Si_3N_4 taper input waveguides as a function of the taper input width, and (b) simulated coupling loss between the input and output taper waveguides as a function of the taper length. The inset in (b) shows the simulated optical field in a 200-μm-long taper for a 0.4 μm input taper width.

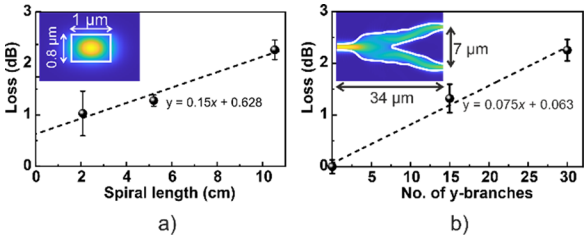

Fig. 5. (a) Measured losses of spiral waveguides of different lengths and (b) measured insertion loss versus the number of Y-branches. The inset in (a) shows a simulated single transverse mode field in a strip waveguide, and that in (b) shows the simulated field profile in a PID-optimized Y-branch.

mismatch loss of ~0.85 dB is obtained for 0.4-μm-wide taper input width. To further study the effect of taper length on the coupling between the taper input and output waveguide modes, the simulations were performed for different taper lengths. The Ansys Lumerical Eigenmode Expansion (EME) solver was used for these simulations and the results are shown in Fig. 4(b) for three different input taper widths. The most efficient taper design gives a single TE mode coupling loss as low as 0.1 dB for a 100 μm taper length. Figure 4(b) shows that minimum coupling loss as a function of taper length is higher for edge couplers with narrow taper widths. This is due to the large mode mismatch loss between RSOA and a narrow taper input, as well as the strong overlap of the optical mode of the narrow taper waveguide with the SiO_2 claddings, which increases the absorption loss during propagation through the taper length.

To ensure stable single-mode operation, the power coupling coefficient was chosen carefully by simulating the Vernier response as a function of the RR coupling gap. Key Vernier parameters like the side-mode suppression ratio (SMSR), resonance linewidth, and transmission loss as a function of coupling gap are shown in the Supplement 1 (Fig. S1). The simulation results are discussed in detail in the Supplement 1. Based on the simulation results, a coupling gap of 850 nm was chosen for the Vernier PIC.

The propagation loss of the strip waveguide was measured with the cut-back method, where a set of three spirals with different lengths and uniform bend radii of 100 μm were fabricated. The loss of these spirals was measured with respect to a straight waveguide reference using a Norcada DFB laser at 2

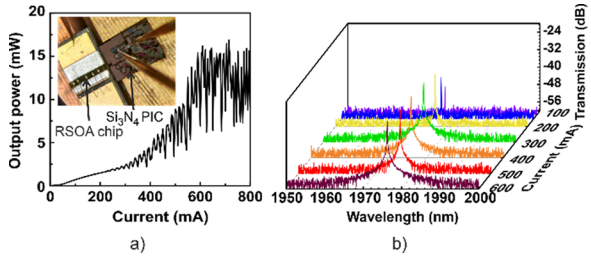

Fig. 6. Measured (a) LI characteristic curve and (b) spectra of the hybrid laser at different CW injection currents. Inset in (a) gives a top camera view of the edge-coupled GaSb RSOA gain chip and the Si_3N_4 PIC.

μm wavelength. The waveguide loss as a function of the spiral length is shown in Fig. 5(a), where the inset shows a simulated single TE mode of the strip waveguide. Fitting a linear curve yields a waveguide propagation loss of 0.15 dB/cm. Since the measured propagation loss also includes scattering losses, it is larger than the simulated propagation loss value. The y intercept of the linear fit gives a 0.008 dB/90° bend loss. To characterize the Y-branch splitter, cascades of 15 and 30 Y-branches in series were fabricated, and their loss was measured with respect to a straight waveguide. By fitting a linear function to the measured loss values, an insertion loss of 0.075 dB was measured at 2 μm, which is close to the simulated (0.05 dB) value. The inset in Fig. 5(b) shows the simulated field profile of an optimized Y-branch designed through PID and fabricated in this work.

To realize the GaSb/Si_3N_4 hybrid laser, a 2-mm-long RSOA gain chip was mounted p-side down on an aluminum nitride (AlN) submount stabilized at 23°C using a thermoelectric temperature control system. The RSOA and the Vernier PIC were brought as close together as possible for efficient end-fire coupling. The continuous wave (CW) current was injected into the RSOA with probe needles, and the output of the hybrid laser was coupled into a multimode (MM) fiber that was connected to a photodiode. The measured light–current (LI) curve is shown in Fig. 6(a). The laser emits up to 15 mW CW output power and has a threshold current below 100 mA. The strong kinks in the LI curve are explained by the phase-matching oscillation between the RSOA and the Si_3N_4 cavities formed when the phase of the RSOA changes with the input current. By tuning the intracavity thermal PS for each input current, efficient phase matching can be achieved. This is shown in the Supplement 1 (Fig. S2), where the PS heater is driven for each input to obtain an optimum phase-matched LI curve. The output power and threshold current are expected to improve upon changing the taper input width (0.2 μm) used in this work to the optimum value (0.4 μm). The phase-matched spectra measured at different gain currents in Fig. 6(b) show the wavelength locking at a current as low as 100 mA with an SMSR of up to 25 dB.

The emission wavelength is tuned by driving the thermal heater over one of the RRs. Figure 7(a) shows the superimposed laser emission spectra achieved by tuning only one RR up to 350 mW drive power. The current injected into the RSOA was kept at 600 mA during the measurements. Changing the temperature of one of the RRs shifts its transmission spectrum and thus the overlapping wavelength jumps from one transmission peak of the unheated RR to the next. The spacing between these peaks is found to be ~3.11 nm, which corresponds to the FSR of the unheated ring. The laser shows a tuning range of over

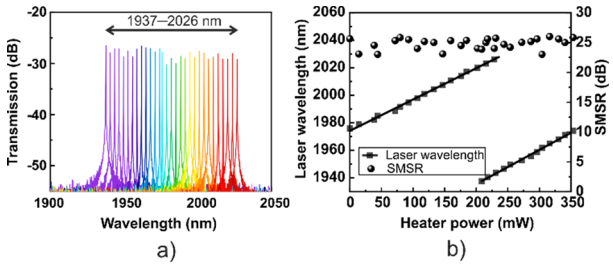

Fig. 7. (a) Superimposed emission spectra of the laser tuned by varying the RR heater power, and (b) wavelength tuning as a function of the heater power, and the SMSR across the entire tuning range.

89 nm, covering the wavelengths between 1937 nm to 2026 nm, which is, to the best of our knowledge, the highest reported for hybrid Vernier lasers around 2 μm in wavelength. The dependence of the lasing wavelength on the power dissipated in the heater is shown in Fig. 7(b). Wavelength scanning across the tuning range of 89 nm is obtained with a heater power consumption of ~ 350 mW. Therefore, the thermal tuning efficiency is 0.25 nm/mW. The SMSR corresponding to each lasing wavelength is also shown in Fig. 7(b). It can be seen that the laser exhibits an SMSR of more than 20 dB across the entire tuning range. The linewidth of the laser, which is limited by the resolution of the spectrum analyzer, is estimated to be < 0.05 nm.

In conclusion, we have demonstrated for the first time, to the best of our knowledge, a widely tunable GaSb/Si_3N_4 hybrid laser with a wavelength of around 2 μm. The laser employs the Vernier mechanism between two thermally tunable ring resonators for wavelength filtering and tuning. The hybrid laser exhibited a relatively high CW output power of 15 mW, a low threshold current of 100 mA, and a broad tuning range of ~90 nm, covering the wavelengths between 1937 nm to 2026 nm. The Vernier PIC is based on ultralow-loss Si_3N_4 building blocks around 2 μm. In fact, we measured 0.15 dB/cm propagation loss for the straight waveguides, 0.008 dB/90° bend loss, and 0.075 dB for the Y-branch insertion loss. In the future, the performance of the hybrid laser will be improved by increasing the coupling efficiency through an optimized taper geometry. The output power can also be increased by using PIC as the output channel or leaving the rear facet of RSOA as-cleaved instead of high-reflection coated. Finally, the emission wavelength will be extended beyond 2 μm to cover the needs of PIC-based hybrid lasers for sensing applications in the 2–3 μm range.

Funding. Academy of Finland (320168); Business Finland (44761, 1613).

Acknowledgments. The authors wish to thank MSc. Jarno Reuna for the preparation of the ARCs/HRCs and Ms. Mariia Bister for wafer-level fabrication of the RSOA.

Disclosures. The authors declare no conflicts of interest.

Data availability. Data underlying the results presented in this paper are not publicly available at this time but may be obtained from the authors upon reasonable request.

Supplemental document. See Supplement 1 for supporting content.

REFERENCES

1. R. Jones, P. Doussiere, J. B. Driscoll, W. Lin, H. Yu, Y. Akulova, T. Komljenovic, and J. E. Bowers, IEEE Nanotechnology Mag. **13**, 17 (2019).
2. S. Fathololoumi, D. Hui, and S. Jadhav, *et al.*, J. Lightwave Technol. **39**, 1155 (2021).
3. A. Hänsel and M. J. R. Heck, JPhys Photonics **2**, 012002 (2020).
4. X. Jia, J. Roels, R. Baets, and G. Roelkens, Sensors **21**, 5347 (2021).
5. P. T. Lin, H. G. Lin, Z. Han, T. Jin, R. Millender, L. C. Kimerling, and A. Agarwal, Adv. Opt. Mater. **4**, 1755 (2016).
6. I. E. Gordon, L. S. Rothman, and C. Hill, *et al.*, J. Quant. Spectrosc. Radiat. Transfer **203**, 3 (2017).
7. R. Wang, A. Malik, I. Šimonytė, A. Vizbaras, K. Vizbaras, and G. Roelkens, Opt. Express **24**, 28977 (2016).
8. J. X. B. Sia, W. Wang, Z. Qiao, X. Li, T. X. Guo, J. Zhou, C. G. Littlejohns, C. Liu, G. T. Reed, and H. Wang, IEEE J. Quantum Electron. **56**, 2001311 (2020).
9. R. Wang, S. Sprengel, A. Vasiliev, G. Boehm, J. Van Campenhout, G. Lepage, P. Verheyen, R. Baets, M.-C. Amann, and G. Roelkens, Photonics Res. **6**, 858 (2018).
10. S. A. Miller, M. Yu, X. Ji, A. G. Griffith, J. Cardenas, A. L. Gaeta, and M. Lipson, Optica **4**, 707 (2017).
11. P. Muñoz, P. W. L. Van Dijk, D. Geuzebroek, M. Geiselmann, C. Dominguez, A. Stassen, J. D. Domenech, M. Zervas, A. Leinse, C. G. H. Roeloffzen, B. Gargallo, R. Banos, J. Fernandez, G. M. Cabanes, L. A. Bru, and D. Pastor, IEEE J. Sel. Top. Quantum Electron. **25**, 8200513 (2019).
12. S. P. Ojanen, J. Viheriala, N. Zia, E. Koivusalo, J. Hilska, H. Tuorila, and M. Guina, *Conf. Dig. - IEEE Int. Semicond. Laser Conf.*, Shimane, Japan,October 16, 2022 .
13. C. A. A. Franken, A. van Rees, L. V. Winkler, Y. Fan, D. Geskus, R. Dekker, D. H. Geuzebroek, C. Fallnich, C. Fallnich, P. J. M. van der Slot, K.-J. Boller, and K.-J. Boller, Opt. Lett. **46**, 4904 (2021).
14. D. Z. Garbuzov, R. U. Martinelli, H. Lee, R. J. Menna, P. K. York, L. A. DiMarco, M. G. Harvey, R. J. Matarese, S. Y. Narayan, and J. C. Connolly, Appl. Phys. Lett. **70**, 2931 (1997).
15. D. Z. Garbuzov, H. Lee, V. Khalfin, R. Martinelli, J. C. Connolly, and G. L. Belenky, IEEE Photonics Technol. Lett. **11**, 794 (1999).
16. C. Lin, M. Grau, O. Dier, and M. C. Amann, Appl. Phys. Lett. **84**, 5088 (2004).
17. M. Geiselmann, in *SPIE Optoelectronics and Photonics Conference (OPTO)* (SPIE, 2021), 11689, paper 116890D.
18. "Ansys Lumerical Photonics Simulation & Design Software, " Ansys Lumerical, 2022 https://www.ansys.com/products/photonics.
19. K. Oda, N. Takato, and H. Toba, J. Lightwave Technol. **9**, 728 (1991).
20. D. G. Rabus, *Integrated Ring Resonators: The Compendium* (Springer, 2007).